sustainability

MDPI

Article

Effect of Aggregate Mix Proportion on Static and Dynamic Mechanical Properties and Pore Structure of Alkali-Activated Slag Mortar with Sludge Pottery Sand

Yuhang Shi, Qinyong Ma *, Dongdong Ma, Kun Huang and Yuqi Gu

School of Civil Engineering and Architecture, Anhui University of Science and Technology, Huainan 232001, China
* Correspondence: qymaah@126.com

Abstract: The overexploitation of river sand will reduce the stability of the river. Using sludge pottery sand (SPS) as a substitute for fine aggregate in mortar can reduce the weight of building mortar and achieve pollution control and resource regeneration. Based on the consideration of energy-saving and carbon reduction, the combination of alkali-activated slag cementitious material and SPS with potential pozzolanic activity to prepare sludge pottery sand alkali-activated slag mortar (PSAM) can replace the traditional silicate river sand mortar. The static and dynamic peak stress of PSAM was tested, and the energy dissipation characteristics of PSAM specimens under the dynamic load were analyzed by using the wave acquisition system of a split Hopkinson pressure bar. The results show that the SPS with 0.15~2.36 mm has better mechanical properties. The increase in the mixing ratio with the SPS with 2.36~4.75 mm will gradually reduce the static and dynamic compressive strength of the specimen, and also reduce the density of the specimen. SEM images and binary pore morphology images showed that the increase in SPS size will lead to a large number of coherent pores inside the specimen, which will increase the air content of the specimen, but at the same time reduce the absorption capacity of the specimen to the wave, so the dynamic energy absorption peak of PSAM appears to decrease significantly. The image of ultra-high-speed photography revealed the mechanism of crack propagation of the PSAM specimen. The development of the crack is positively correlated with the dynamic energy absorption performance when the specimen is completely broken.

Keywords: alkali-activated slag; sludge pottery sand; split Hopkinson pressure bar; ultra-high-speed photography; mechanical properties

Citation: Shi, Y.; Ma, Q.; Ma, D.; Huang, K.; Gu, Y. Effect of Aggregate Mix Proportion on Static and Dynamic Mechanical Properties and Pore Structure of Alkali-Activated Slag Mortar with Sludge Pottery Sand. *Sustainability* **2023**, *15*, 2771. https://doi.org/10.3390/su15032771

Academic Editor: Jun Wang

Received: 3 January 2023
Revised: 18 January 2023
Accepted: 31 January 2023
Published: 3 February 2023

1. Introduction

The most commonly used sand in building mortar is natural river sand [1]. River sand has good mechanical properties and low mud content, and it is easy to obtain [2]. However, the overexploitation of natural river sand will lead to a series of environmental problems [3,4]. Therefore, the research on fine aggregate substitutes in building mortar is very diverse [5]. Since mortar is made by mixing cementitious materials and fine aggregate, fine aggregate not only has excellent mechanical properties, but also has good compatibility with cementitious materials [6].

Among the artificial fine aggregates, pottery sand is considered to be an energy-efficient and environmentally friendly building material [7]. Pottery sand is a small-sized ceramsite with a particle size of 0.15~4.75 mm, which is calcined in a high temperature environment by a variety of silicate and aluminum metal salt minerals and foaming agents. It has the advantages of light weight, high strength, stable chemical properties, and the artificial regulation of physical and mechanical properties [8]. In addition, pottery sand is widely used as water treatment filter material and petroleum fracturing proppant [9].

The production mode of pottery sand has the characteristics of regionality and diversity. The use of low-cost local mineral or industrial solid waste results in using rotary kiln

high-temperature firing [10,11]. For some solid wastes of clay-like mineral composition, firing them into pottery sand is not only environmentally friendly, but also economically beneficial [12]. There are many solid wastes that can be used to burn ceramsite and pottery sand, such as coal gangue, heavy metal tailings, and municipal sludge [8,13]. Zhang et al. [14] used a mixture of biochar and sewage sludge incineration ash as a lightweight building material added to concrete. Yu et al. [15] made super sewage sludge light environmental ceramsite and analyzed the synthesis mechanism of it.

Among the abovementioned solid wastes, municipal sludge is one of the pollutions that every city and community has to face together [16]. Therefore, the effective utilization of this kind of waste produced by the water supply and drainage plants to make sludge pottery sand (SPS) plays an important role in the water safety of urban residents and the prevention and control of local water and soil resource pollution [17]. At present, the common process is to mix it with a foaming agent and binder, and at a high temperature of 1100~1400 °C, it presents a molten glass state and produces a large number of expansion pores [18,19]. After cooling, a stable sludge pottery sand can be obtained. Although it consumes a certain amount of fuel in the process of thermal processing, in fact, this turns the sludge from a harmful solid waste into a usable lightweight building material, and the heat consumed in the production process is not more than other types of artificial pottery sand. Therefore, SPS reduces the actual energy consumption from the perspective of saving waste treatment costs [20].

As a new type of building material, alkali-activated slag mortar has a good phase with the SPS while effectively replacing ordinary Portland cement mortar. Chang et al. [21] studied the potential volcanic ash activity of sludge. Therefore, in the process of the setting and hardening of alkali-activated slag paste, the substances in the SPS will not have an antagonistic effect on the hydration products, and they have a positive effect on the performance of the interface transition zone [22]. The comprehensive performance of sludge ceramsite alkali-activated slag mortar (PSAM) composed of the SPS and alkali-activated slag paste was studied, which has a positive role in promoting the application of SPS as an environmentally friendly building material [23,24].

In the present study, Jiao et al. [25] explored the effect of an alkaline activator on the performance of ceramic sand to alkali-activated slag paste. Xie et al. [26] used a sludge lightweight aggregate and alkali-activated slag materials to partially replace sand and Portland cement to make non-bearing structural concrete with an application value; however, for the SPS, a fine aggregate with large pores inside, the performance of its porous structure under dynamic loading is worth exploring. As a kind of material with a short setting time and fast strength growth [27], the static and dynamic mechanical properties of alkali-activated slag mortar using ordinary river sand have been widely studied [28]; however, the research on the static and dynamic mechanical properties of PSAM is relatively lacking. In view of the large difference between the strength and apparent density of different kinds of ceramic sand, it is valuable to study the static and dynamic mechanical properties of PSAM for the subsequent modification and enhancement of the SPS aggregate.

This paper innovatively uses the SPS and slag to prepare low-density alkali-activated slag mortar, and quantitatively analyzes the static and dynamic mechanical properties and energy absorption characteristics of the lightweight aggregate mortar completely composed of pottery sand. The static strength of the SPS was quantified by a cylinder pressure test, and the relationship between the apparent density of the SPS and the static and dynamic strength of PSAM specimens was analyzed. The split Hopkinson pressure bar (SHPB) test system can collect and process the peak compressive strength and energy absorption characteristics of PSAM under the dynamic load, which can systematically reflect the dynamic mechanical properties and energy absorption characteristics of PSAM [29]. The images collected by the ultra-high-speed camera can accurately determine the crack evolution process and specimen breakage of PSAM under the dynamic load [30].

In the experiment, the size of the SPS was taken as the main variable, and the static and dynamic mechanical properties of PSAM with different aggregate size ratios were tested. The energy dissipation law and crushing morphology of the specimens in the dynamic compression experiment were analyzed [31,32]. The images collected by the electron microscope and the hardened pore-measuring instrument were comprehensively evaluated. The influence of the pore structure of the SPS on the strength and energy absorption characteristics of PSAM specimens was analyzed from the micro level, and the characteristics of the interface transition zone between the SPS and alkali-activated slag paste were analyzed.

2. Test Materials and Methods

2.1. Preparation for SPS

The SPS, which was successfully fired in the rotary kiln, was taken out and screened. The main elements of the SPS are shown in Table 1, and the main components were sludge and clay. The SPS after screening was divided into three particle sizes: 0.15~2.36 mm, 2.36~4.75 mm, and coarse ceramsite larger than 4.75 mm. Dry balls larger than 9 mm and debris smaller than 0.15 mm were removed from the SPS to avoid affecting its stability. The screened SPS and coarse ceramsite were washed and dried, and the cylinder pressure strength test and apparent density test were carried out. The test results are shown in Table 2.

Table 1. Main elements of SPS.

Element	O	Si	Al	Fe	K	Ca	Na	Ti	Mg	Mn	P	Cl
%wt	48.22	32.03	7.95	4.85	2.96	1.31	0.93	0.75	0.61	0.13	0.09	0.05

Table 2. Parameters of SPS.

Particle Size Range	0.15~2.36 mm	2.36~4.75 mm	4.75~9 mm
Apparent density (kg/m^3)	1.121	0.984	0.826
Cylinder compressive strength (MPa)	12.1	7.38	4.95

2.2. Experimental Instruments and Testing Items

Before pouring the specimen, the SPS needed to be immersed in water 24 h in advance to prevent surface water absorption when in contact with the alkali-activated slag paste. The main raw material of the alkali-activated slag paste was S95 grade granulated blast furnace slag powder, and a small amount of SiO_2 non-encrypted silica fume with a purity of 96% was used to adjust the viscosity of the alkali-activated slag mortar. The mass ratio of the activator used in the experiment, the alkali-activated slag paste solution solid ratio, was 0.53. The water glass modulus was 3.3, the water was normal-temperature drinking water, and the caustic alkali used the powder analysis pure reagent. The slag and silica fume were fully mixed in a stirrer, and the activator was added at 23 °C. After the slurry was prepared, the SPS was added and stirred continuously until the SPS was completely wrapped by the slurry. The specimens were cured in a saturated calcium hydroxide solution at 23 °C for 28 days. In order to carry out the static uniaxial compression test of PSAM, it was necessary to cast a cube specimen with a side length of 50 mm [33]. The static compressive strength of the specimen was measured on a hydraulic servo press test device.

In the dynamic impact test, the production and curing process of PSAM was consistent with the above static test, but the size of the specimen was a cylindrical specimen with a diameter of 50 mm and a height of 25 mm. This was to be consistent with the diameter of the loading system of the impact test. The SHPB test system is shown in Figure 1. The strain of the rod was measured by a resistance strain gauge. The experimental impact pressure was set to 0.3 MPa. The electrical signal will be converted into a waveform through the

processing system, and the peak stress and dynamic dissipation energy of the experiment can be obtained by analyzing the waveform.

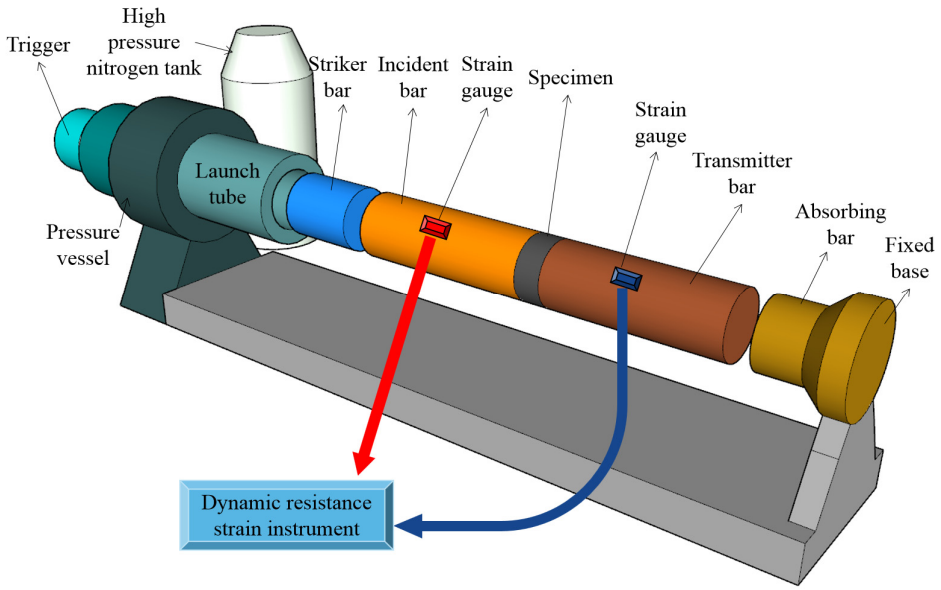

Figure 1. SHPB system.

During the experiment, an ultra-high-speed camera was used to take photos of the impact-crushing process of the specimen. The frame rate of the ultra-high-speed camera was set to 30,030 frames per second, and the images taken were black and white images with a resolution of 384 × 608. The device had a pre-trigger function, and the trigger was triggered when the specimen was subjected to dynamic load, but the camera can collect all the data before and after the trigger. The first frame of the crack in the specimen can be observed in the image acquisition software, which was used as the starting frame of the failure process until the specimen was completely destroyed in the subsequent impact process. Therefore, the high-speed camera image can completely record the failure process of the specimen. It was necessary to use a high-intensity fill light to take photos of the specimen. The actual arrangement of the device of the ultra-high-speed camera system was shown in the picture. The instrument began shooting when the specimen did not receive an impact and stopped collecting after the specimen was completely destroyed.

After the impact test, the fragments of the PSAM specimen were recovered. The PSAM sample was placed in isopropanol to replace the internal moisture, and the sample was dried in a vacuum container for SEM testing. The interior of the SPS contains abundant pores, so the interior of PSAM also contains abundant pores. The pore-measuring instrument was used to collect and analyze the image of the cross-section of PSAM. The experimental system is shown in Figure 2. It had the ability to collect real images and binarize the images, and it could intuitively characterize the pore structure morphology of the cross-section of the specimen.

2.3. Experimental Mix Ratio

In this experiment, the SPS accounted for 60% of the total volume of the specimen. In order to study the effect of the average particle size of the SPS on the static and dynamic mechanical properties of PSAM, two kinds of ceramic sand were classified in the experiment. The SPS with 0.15~2.36 mm was named as X, and the SPS with 2.36~4.75 mm was named as Y. The volume ratio of the two was taken as the variable, and a total of six experimental groups are shown in Figure 3. At the same time, in order to verify the integrity of the data, coarse ceramsite and SPS were mixed according to the appropriate apparent volume ratio, and six reference groups were set-up to study the change trend of the SPS aggregate size to further increase the compressive strength of PSAM.

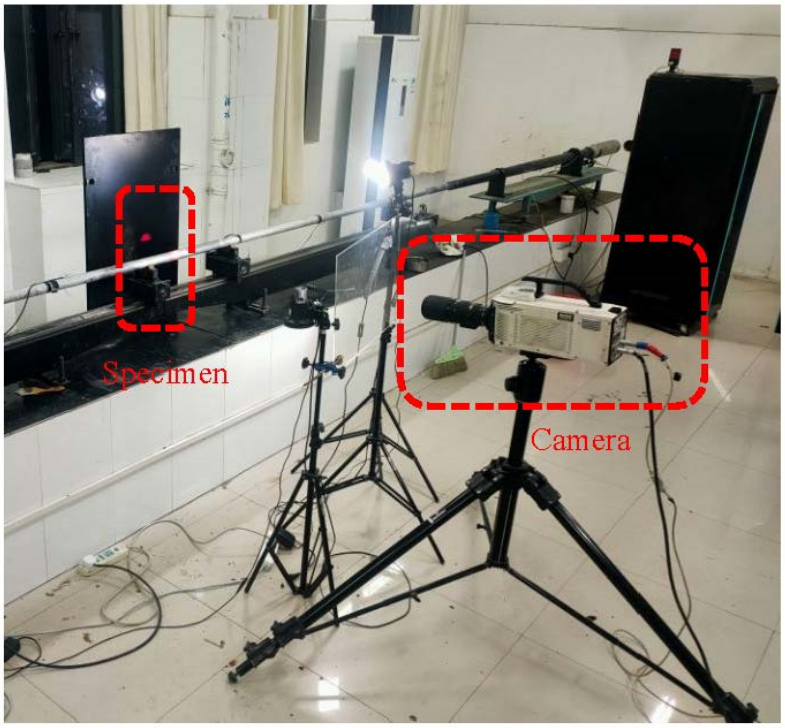

Figure 2. Ultra-high-speed camera system.

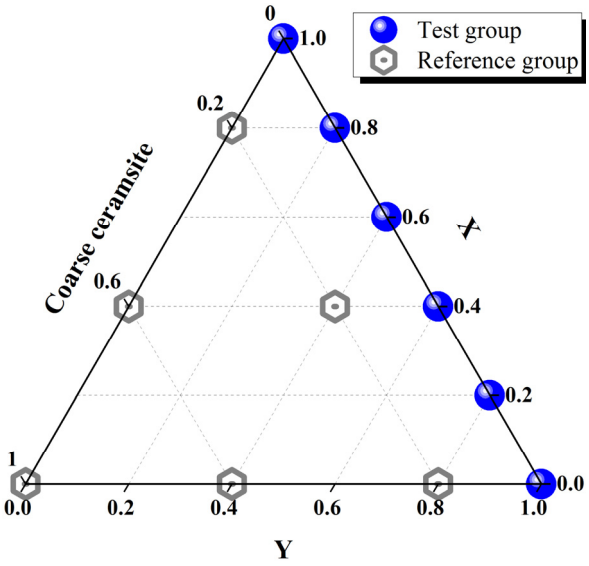

Figure 3. Mix ratio of PSAM.

3. Experimental Results and Discussion

3.1. Static Mechanical Properties

The static compressive strength of the PSAM test group and the reference group is shown in Figure 4. The static compressive strength of the X_1Y_0 group is 33.74 MPa, which is the highest value in the experimental group, and the lowest value appears in the X_0Y_1 group, which is only 52.4% of the X_1Y_0 group. Therefore, the PSAM specimen with 0.15 mm~2.36 mm SPS has the best static compressive performance, which is consistent with the static compressive strength of the SPS. It can be seen from the data of the six reference groups that the static compressive strength of the specimens with coarse ceramsite instead of the SPS is 73.8% lower than that of X_1Y_0 group, indicating that large-sized ceramsite is the weak link of the overall structure in PSAM. Therefore, considering the

static mechanical properties, the use of PSAM to prepare lightweight concrete should not use large-sized sludge ceramsite coarse aggregate. In Figure 4, the aggregate ratio of the X group and Y group is regarded as the independent variable, and the static compressive strength (σ_s) is regarded as the dependent variable. The influence of the change of the aggregate volume ratio on the static compressive strength can be fitted by a quadratic equation. The fitting result and R2 value are given in the diagram, so the quadratic equation can be used to fit the data law. The reason for this data pattern is that the static compressive strength of PSAM decreases with the increase in SPS size, but the rate of strength reduction decreases with the increase in SPS size. The decrease in aggregate strength and the increase in the uneven mortar system are the main causes of this phenomenon.

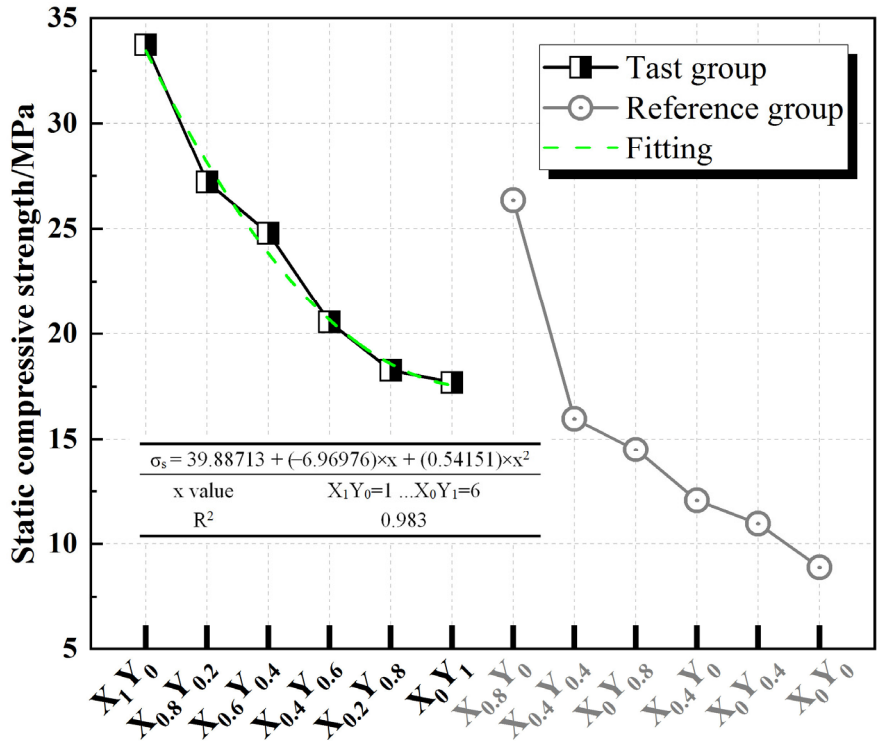

Figure 4. Static compressive strength of PSAM.

Because the total volume is the same, the volume ratio of the SPS and coarse ceramsite of the X-type and Y-type in SSAM can be set as three coordinate axes, and a three-term data space can be obtained. The height in the space is the strength value. The non-linear surface fitting of the data points in the three-phase space of the SPS volume ratio and static compressive strength is carried out. The basic unit of the model is quadratic, and the fitting results are shown in Figure 5. The main factors of the model are analyzed. The R^2 value is 0.989, approaching 1. The non-linear regression model can better predict the data trend of static compressive strength caused by aggregate size variables in the SPS.

Due to the difference in size, the traits of the X-type and Y-type SPS are not completely consistent. Although the gap of the SPS cylinder compressive strength data is one of the factors of the change of static compressive strength, the static strength ratio of X_1Y_0 and X_0Y_1 can not be simply explained by the difference in aggregate strength; otherwise, the fitting law of the above data would be approximately linear. The difference in pore structure is a potential factor in the influence of these two SPSs on strength, which can be analyzed from two aspects. One is the difference in pore size. In the case of a certain porosity of concrete, the larger the average size of all independent bubbles, the less the total number of bubbles, and the negative impact on the strength is obvious. The average pore size of the X-type SPS is much smaller than that of the Y-type SPS, and the static compressive strength of the SPS is lower than that of the alkali-activated slag paste. Therefore, the

Y-type SPS is more likely to become a weak point in the compression test than the X-type SPS in PSAM. However, the macropores still have a positive effect, that is, the saturated SPS has a slow-release effect of water. Because the SPS can be well-dispersed in PSAM and the water storage is moderate, the SPS can play a good internal curing role in PSAM, reduce the internal reaction exothermic temperature peak in the middle and late stages of the alkali-activated slag hydration reaction, supplement in a timely manner the evaporated water, and reduce the generation of internal microcracks. Therefore, from the perspective of the internal curing effect, the Y-type SPS has a more positive effect on the hydration reaction of PSAM.

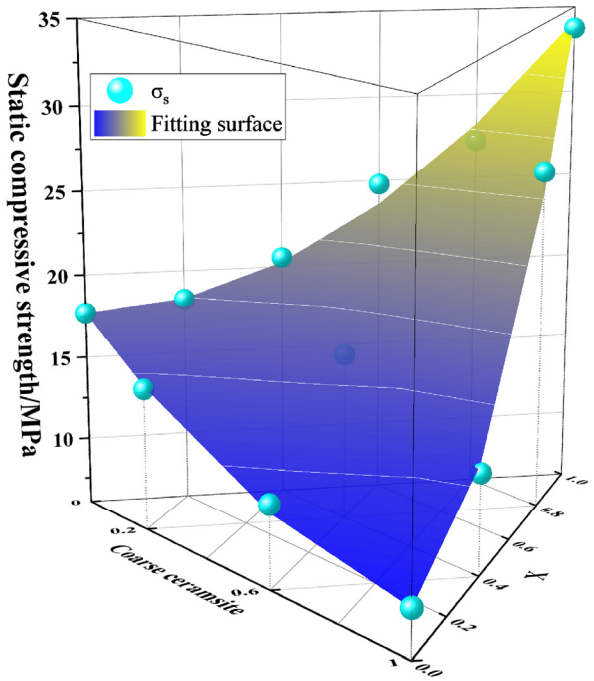

Figure 5. Non-linear surface fitting of σ_s.

On the other hand, the performance of the interfacial transition zone between the SPS and paste is an important part of the overall strength of PSAM. The concentration of alkali metal ions and hydroxide ions in the two-component activator is higher, so it has higher ion osmotic pressure, which is also the most important way for the water stored in the SPS to be replaced. Therefore, in the early stage of hydration reaction, ITZ exists in the paste with low solid solubility and high fluidity. This will cause its static compressive strength to be slightly lower than that of the paste away from the SPS, but its high fluidity will also help it penetrate into the pores and cracks on the SPS surface and avoid bubbles adhering to the SPS surface. Since the X-type SPS has a finer particle size and a larger contact area with the paste at the same volume, although the total area of the ITZ increases, tight contact between the aggregate and the paste reduces this negative effect.

The cross-section of the PSAM specimen in the static compression test is shown in Figure 6. It can be observed that although ITZ is the contact zone between the aggregate and paste, the breakage of the specimen must be induced by the failure of SPS strength, and ITZ does not have an obvious peeling phenomenon with SPS on the fracture surface. In the X group and the Y group, there is often a relatively thick skeleton structure inside, which makes it have better force transmission ability when subjected to load. The coarse ceramsite introduces a large-size cavity in the PSAM, which will lead to internal stress concentration when subjected to load, further accelerating the destruction of the specimen.

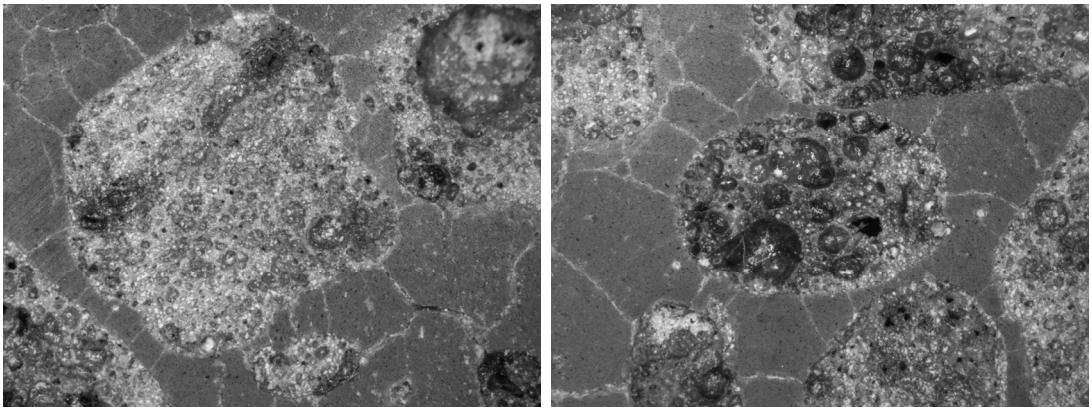

Figure 6. Section morphology of specimen.

3.2. Dynamic Compressive Strength

The SHPB impact compression test is carried out on PSAM specimens, and the peak compressive strength can be collected as shown in Figure 7. The dynamic compressive strength of the X_1Y_0 group is 27.89 MPa, and the lowest dynamic compressive strength of the X_0Y_1 group is 16.29 MPa. The dynamic compressive strength of PSAM specimens with the X-type SPS is 171.2% of that with the Y-type SPS, which is consistent with the data trend of the static compressive strength of the PSAM. The data of the six reference groups also show further decline, and the dynamic mechanical properties of coarse ceramsite in the alkali-activated slag paste are still the lowest. In addition, this negative effect is deeper than the static compressive strength. In Figure 6, the aggregate ratio of X and Y is regarded as the independent variable, and the dynamic compressive strength (σ_d) is regarded as the dependent variable. The influence of the change of the aggregate volume ratio on the dynamic compressive strength can be fitted by the quadratic equation. The fitting result and R^2 value are given in the diagram; therefore, the quadratic fit is accurate in predicting data trends.

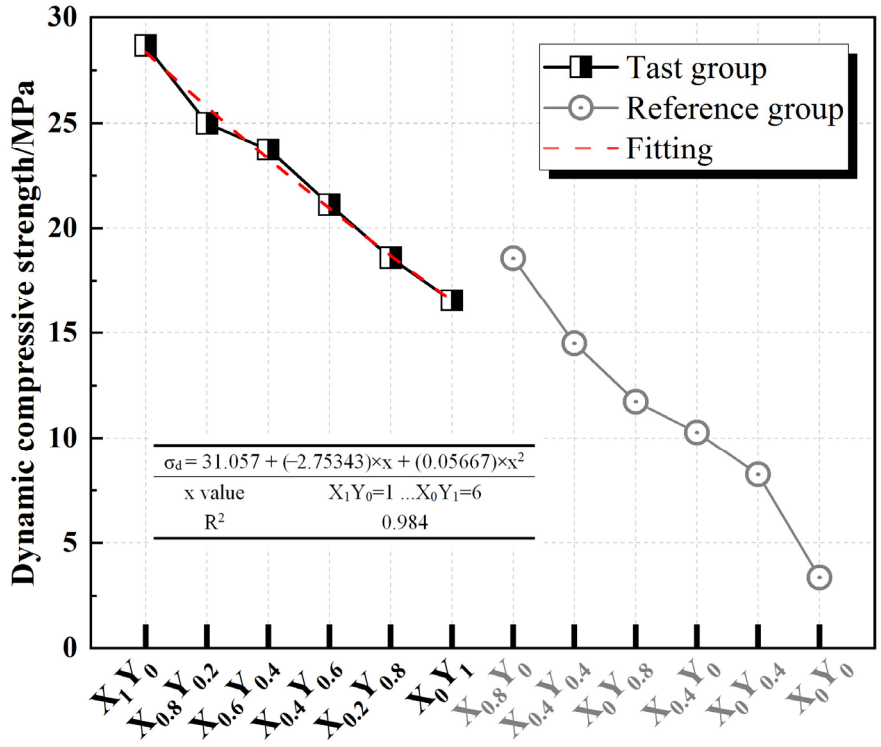

Figure 7. Dynamic compressive strength of PSAM.

The volume ratio of the X-type and Y-type SPS and coarse ceramsite in SSAM is set as three coordinate axes, and the height in space is the dynamic compressive strength value. Thus, a three-phase space scatter diagram can be drawn, and non-linear surface fitting can be performed on the data points of the SPS volume ratio and dynamic compressive strength in the coordinate space. The basic unit of the model is a quadratic form, and the fitting results are shown in Figure 8. The main factor significance analysis of the model reveals that the R^2 value is 0.982, approaching 1. The non-linear regression model can better predict the data trend of static compressive strength caused by aggregate size variables in the SPS.

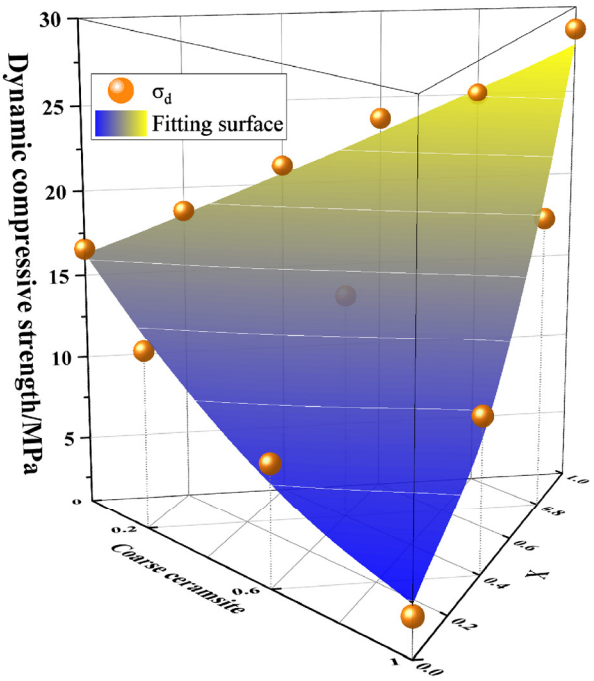

Figure 8. Non-linear surface fitting of σ_d.

3.3. Failure Morphology and Dynamic Absorption Energy

The dynamic impact test will cause the specimen to break and produce a large number of fragments. This process starts from axial compression and ends at the same time as the radial tensile failure and axial compression failure. The impact process of the PSAM specimen is collected and recorded in real-time by the ultra-high-speed camera. The failure process of the specimen is shown in Figure 9.

It can be seen from Figure 9 that the X_1Y_0 group with the highest dynamic compressive strength is cracked by axial cracks. After the first crack is born, multiple axial cracks are generated, and the crack width continues to expand. With the further compression of the incident bar on the specimen in the impact test system, the axial crack of the PSAM specimen will develop into a circumferential crack, and the specimen will be further broken until the end of the impact process. The impact process of the X_0Y_1 group with the lowest strength is relatively simple. When the impact load is applied to the specimen by the incident rod, the PSAM specimen undergoes brittle failure, resulting in penetrating the axial main cracks and some oblique fine cracks. Then, the specimen is completely destroyed, and the impact test is completed. These are the two extreme cases in the captured image, corresponding to the maximum and minimum values of the dynamic peak strength when the specimen is destroyed. In summary, the higher the degree of fragmentation of the specimen, the higher the dynamic compressive strength.

The cracks in the specimen during the impact process consume the energy that should be transmitted to the transmission rod. Therefore, the peak value of the impact energy absorbed by the specimen can be obtained by analyzing the waveforms collected by

the transmission rod and the incident rod. The simplified three-wave method is used to calculate and count the peak absorption energy of the specimen during the dynamic load [34]. The calculation results are shown in Figure 10. The trend of the experimental data is positively correlated with the dynamic peak strength, which is also consistent with the diffusion of cracks during the impact process. The dynamic energy absorption of the six reference groups is also listed in Figure 10, and their values are lower than the X_1Y_0 group. Therefore, the increase in SPS size will lead to a decrease in the dynamic energy absorption capacity of the specimen. The aggregate ratio X and Y is regarded as the independent variable, and the dynamic energy absorption (E) is regarded as the dependent variable. The influence of the change of the aggregate volume ratio on the dynamic energy absorption can be fitted by the quadratic equation. The fitting result and R^2 value are approaching 1, so the quadratic equation can be used to fit the data law.

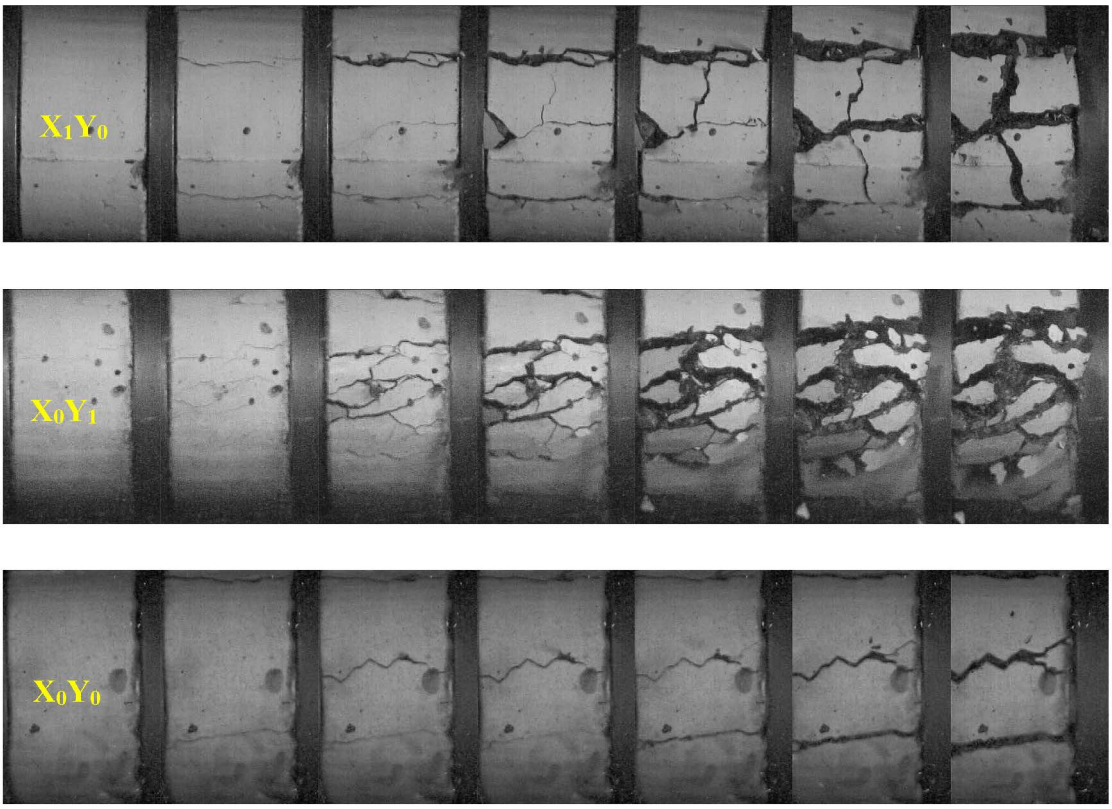

Figure 9. Ultra-high-speed photography.

Because the total volume is consistent, the volume ratio of the X-type SPS, Y-type SPS, and coarse ceramsite in PSAM can be set as three coordinate axes, and a three-term data space can be obtained. The height in the space is the dynamic energy absorption (E). The non-linear surface fitting of the data points in the three-phase space of SPS volume ratio and dynamic energy absorption is carried out. The basic unit of the model is quadratic, and the fitting results are shown in Figure 11. The R^2 value is 0.981, so the non-linear regression model can better predict the data trend of dynamic energy absorption in the SPS.

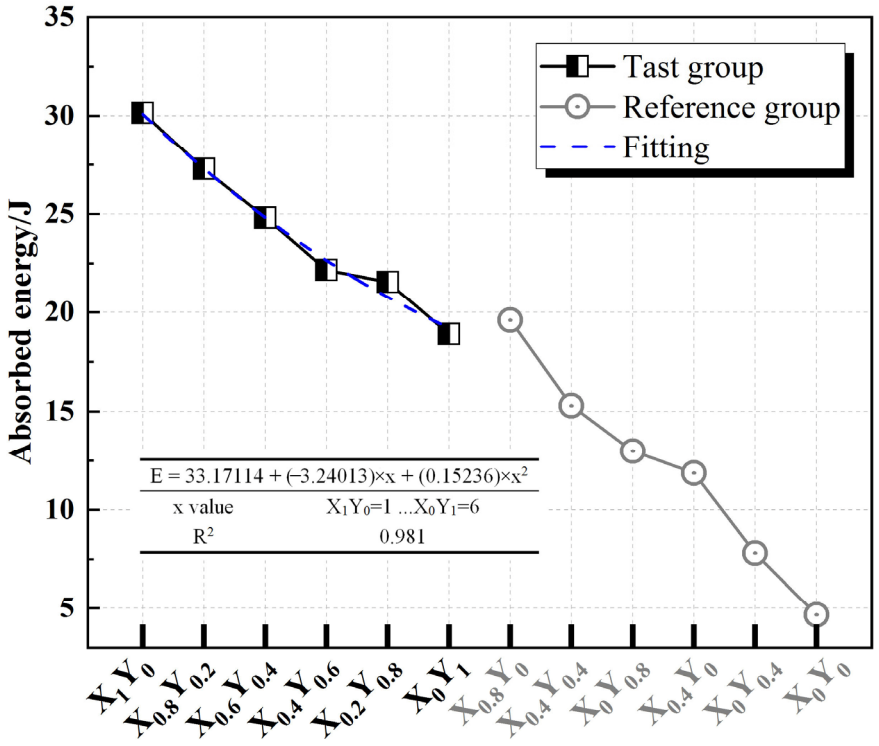

Figure 10. Energy absorption of PSAM.

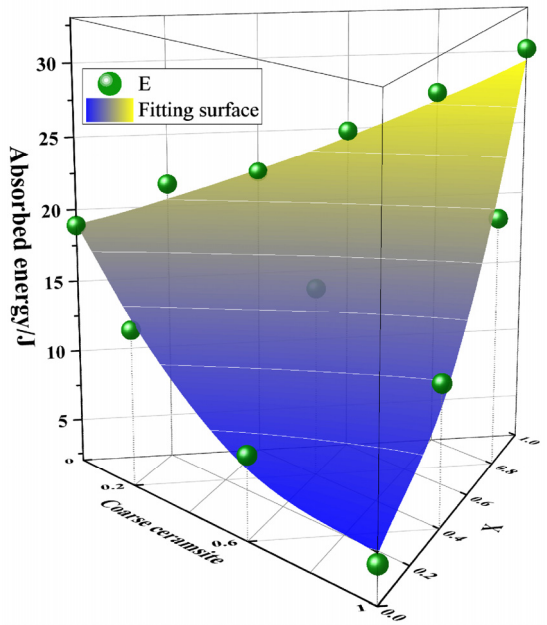

Figure 11. Non-linear surface fitting of E.

4. Pore Morphology and Air Content

The complete PSAM specimen is cut and polished, and then observed under the hardened mortar pore structure-measuring instrument. The binarized acquisition image is shown in Figure 12. The X_1Y_0 group has the best mechanical properties, so its pore structure is more concentrated, and the size of the hole is smaller. The density of bubbles in the X_0Y_1 group is higher than that of the PSAM specimens in the X_1Y_0 group, and the size is larger.

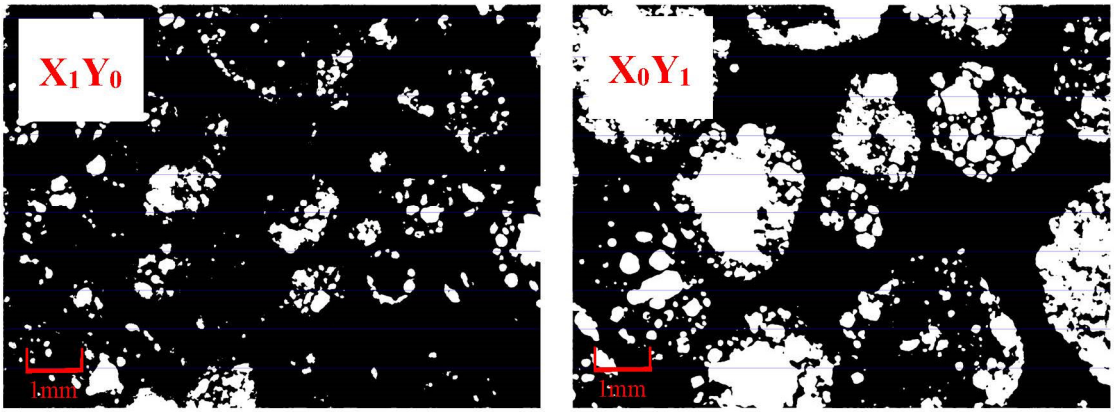

Figure 12. Pore morphology of PASM.

The internal air content of PSAM can be calculated by the average pore chord length and the total number of pores collected by the pore-measuring instrument. The results are shown in Figure 13. It can be found that the size of the SPS significantly affects the air content of the specimen, with the highest group increasing by 252.42% compared to the lowest group. The Y-type SPS will introduce more air into the hardened PSAM due to its large internal cavity. This is because in the SPS firing process, there will be closed pores inside, so the conventional means of saturation can not make the internal gas replaced by water. Moreover, the larger the size of the SPS, the greater the probability and size of the closed pores.

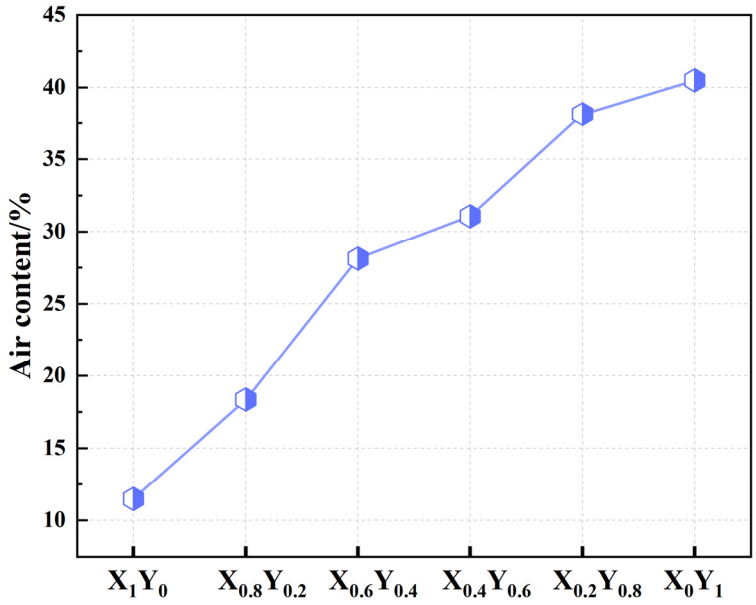

Figure 13. Air content of PSAM.

5. SEM Microscopic Characterization

The microstructure of the PSAM specimen after crushing and coring is shown in Figure 14. It is worth noting that the SPS in Figure 14a is not added to the alkali-activated paste. In this way, the surface morphology of the SPS in the original dry state can be easily observed. The surface of the SPS is full of pores connected with the interior, and the surface texture is more, which further increases the specific surface area of the SPS and increases the roughness of ITZ. Therefore, although the SPS has low strength, it has a better performance in mechanical properties.

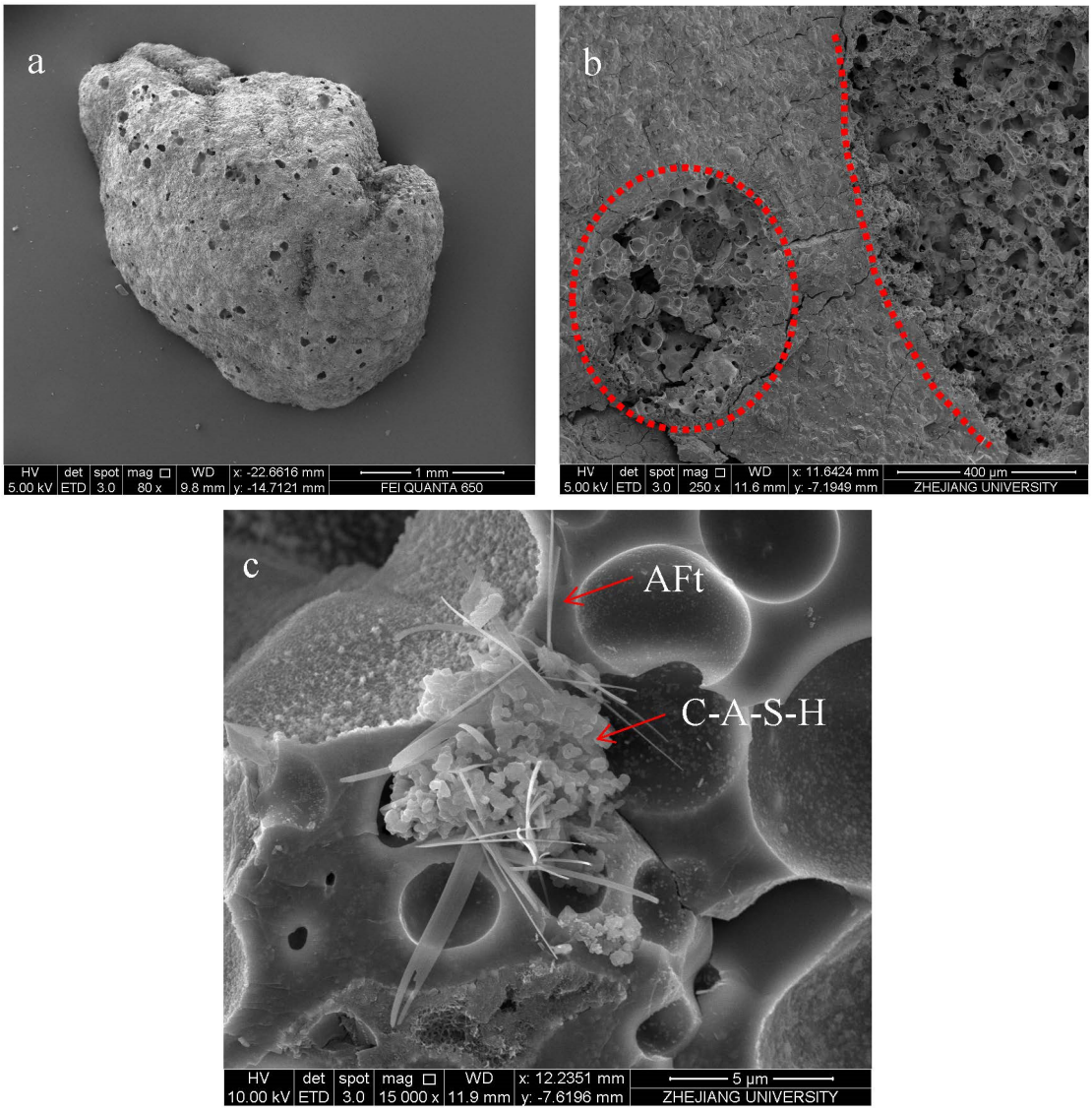

Figure 14. SEM images of PASM. ((**a**): The morphology of the complete SPS. (**b**): The cross section of the specimen, the area of the dotted lines in the figure is the broken SPS. (**c**): Hydration products of specimens).

Figure 14b shows the cross-sectional morphology of the PSAM specimen under impact loading. It can be seen from the figure that the SPS is closely combined with the alkali-activated paste, and the paste is filled in the holes on the outer layer of the SPS and produces a large amount of staggered fibrous C-A-S-H. This dense network structure further enhances the strength of the ITZ. At the cross-section of the damaged specimen, it can be observed that there is a good bite force between the SPS and alkali-activated slag paste. The impact load does not cause the crack to expand to the interface transition zone, but mainly causes the SPS to produce compression failure. Therefore, even if the smaller SPS has more ITZ in the same volume, its performance does not deteriorate significantly. Figure 14c is an enlarged alkali-activated slag particle. The needle-like AFt is interwoven with the cluster-like C-A-S-H, which is the main product of the alkali-activated slag hydration reaction.

6. Conclusions

In order to explore the feasibility of the SPS completely replacing ordinary river sand in alkali-activated slag mortar, static and dynamic uniaxial compressive experiments were carried out on PSAM with various fine aggregate volume ratios. The results show that the

SPS with 0.15~2.36 mm has strong mechanical properties, and the PSAM completely using this SPS has the highest value in the transverse comparison of static and dynamic uniaxial compressive strength.

The static compressive strength of the Y-type SPS is lower than that of the X-type SPS. When it is mixed with alkali-activated slag mortar, the static compressive strength of the X_1Y_0 group is 386.4% of the X_0Y_1 group. The static compressive strength is negatively correlated with the size of the SPS, but they are not linearly correlated. This is because the Y-type aggregate has a strong water storage capacity and plays a positive role in the interfacial transition zone and hydration reaction.

The dynamic compressive strength and dynamic energy absorption peak of the experimental group show a similar change rule to the static compressive strength. The ultra-high-speed camera reveals the characteristics and sequence of crack formation when PSAM is damaged by the impact load. The specimens with higher strength include the PSAM specimens of the X_1Y_0 group. The dynamic compressive capacity and dynamic energy absorption capacity of the SPS with a larger size in the specimen are increasingly reduced, and the larger pores will lead to stress concentration, making the SPS's interior a weak surface.

The pore morphology of the specimen further proves the influence of the pore structure inside the SPS on the strength of the PSAM specimen. The larger SPS is more likely to contain closed large pores, which introduce air into the PSAM and increase the air content of the specimen. The air content is closely related to the energy absorption characteristics and mechanical properties of the specimens. The air content of the X_1Y_0 group is 28.37% of the X_0Y_1 group. In the SEM image, it was found that the alkali-activated slag paste is filled in the outer pores of the SPS and produces hydration products, which indicates that the alkali-activated slag paste has excellent compatibility with the SPS fine aggregate.

In this paper, the mechanical properties and pore structure of PSAM were studied in detail, and there are still some shortcomings. In order to improve the application value of this kind of material, it is necessary to carry-out the research of the durability experiment in the follow-up work to explore the working performance of this kind of environmental-protection building material in a harsh environment. In addition, the improvement of the SPS is also the focus of improving the mechanical properties of mortar, and its pore structure should be further optimized in the manufacturing process.

Author Contributions: Conceptualization, Y.S. and Q.M.; methodology, Y.S.; software, Y.S.; validation, Y.S., K.H. and Y.G.; formal analysis, K.H.; investigation, Y.G.; resources, Y.S.; data curation, Y.S.; writing—original draft preparation, D.M.; writing—review and editing, K.H.; visualization, Q.M.; supervision, K.H.; project administration, D.M.; funding acquisition, Q.M. All authors have read and agreed to the published version of the manuscript.

Funding: This research was funded by a grant from the University Synergy Innovation Program of Anhui Province, China, grant number GXXT-2019-005.

Institutional Review Board Statement: Not applicable.

Informed Consent Statement: Not applicable.

Data Availability Statement: Not applicable.

Conflicts of Interest: The authors declare no conflict of interest.

References

1. Abdel-Gawwad, H.A.; Sanad, S.A.; Mohammed, M.S. A clean approach through sustainable utilization of cement kiln dust, hazardous lead-bearing, and sewage sludges in the production of lightweight bricks. *J. Clean. Prod.* **2020**, *273*, 123129. [CrossRef]
2. Cecconet, D.; Capodaglio, A.G. Sewage Sludge Biorefinery for Circular Economy. *Sustainability* **2022**, *14*, 14841. [CrossRef]
3. Fernandes, A.S.; Azevedo, T.; Rocha, F.; Nunes, E.; Homem, V. Plant uptake potential and soil persistence of volatile methylsiloxanes in sewage sludge amended soils. *Chemosphere* **2022**, *308*, 136314. [CrossRef] [PubMed]
4. Bubalo, A.; Vouk, D.; Stirmer, N.; Nad, K. Use of Sewage Sludge Ash in the Production of Innovative Bricks—An Example of a Circular Economy. *Sustainability* **2021**, *13*, 9330. [CrossRef]

5. Lu, J.X.; Zhou, Y.; He, P.; Wang, S.; Shen, P.; Poon, C.S. Sustainable reuse of waste glass and incinerated sewage sludge ash in insulating building products: Functional and durability assessment. *J. Clean. Prod.* **2019**, *236*, 117635. [CrossRef]
6. Areias, I.O.R.; Vieira, C.M.F.; Colorado, H.A.; Delaqua, G.C.G.; Monteiro, S.N.; Azevedo, A.R.G. Could city sewage sludge be directly used into clay bricks for building construction? A comprehensive case study from Brazil. *J. Build. Eng.* **2020**, *31*, 101374. [CrossRef]
7. Świerczek, L.; Cieślik, B.M.; Konieczka, P. Challenges and opportunities related to the use of sewage sludge ash in cement-based building materials–A review. *J. Clean. Prod.* **2021**, *287*, 125054. [CrossRef]
8. Gu, C.; Ji, Y.; Zhang, Y.; Yang, Y.; Liu, J.; Ni, T. Recycling use of sulfate-rich sewage sludge ash (SR-SSA) in cement-based materials: Assessment on the basic properties, volume deformation and microstructure of SR-SSA blended cement pastes. *J. Clean. Prod.* **2021**, *282*, 124511. [CrossRef]
9. Danish, A.; Ozbakkaloglu, T. Greener cementitious composites incorporating sewage sludge ash as cement replacement: A review of progress, potentials, and future prospects. *J. Clean. Prod.* **2022**, *371*, 133364. [CrossRef]
10. Tang, P.; Xuan, D.; Li, J.; Cheng, H.W.; Poon, C.S.; Tsang, D.C. Investigation of cold bonded lightweight aggregates produced with incineration sewage sludge ash (ISSA) and cementitious waste. *J. Clean. Prod.* **2020**, *251*, 119709. [CrossRef]
11. Chang, Z.; Long, G.; Xie, Y.; Zhou, J.L. Recycling sewage sludge ash and limestone for sustainable cementitious material production. *J. Build. Eng.* **2022**, *49*, 104035. [CrossRef]
12. Świerczek, L.; Cieślik, B.M.; Konieczka, P. The potential of raw sewage sludge in construction industry—A review. *J. Clean. Prod.* **2018**, *200*, 342–356. [CrossRef]
13. Ducoli, S.; Zacco, A.; Bontempi, E. Incineration of sewage sludge and recovery of residue ash as building material: A valuable option as a consequence of the COVID-19 pandemic. *J. Environ. Manag.* **2021**, *282*, 111966. [CrossRef]
14. Zhang, Y.; Maierdan, Y.; Guo, T.; Chen, B.; Fang, S.; Zhao, L. Biochar as carbon sequestration material combines with sewage sludge incineration ash to prepare lightweight concrete. *Constr. Build. Mater.* **2022**, *343*, 128116. [CrossRef]
15. Yu, L.; Zhang, Y.; Mao, H.; Cui, K.; Liu, H. Structure evolution, properties and synthesis mechanism of ultra-lightweight eco-friendly ceramics prepared from kaolin clay and sewage sludge. *J. Environ. Chem. Eng.* **2022**, *11*, 109061. [CrossRef]
16. Singh, J.; Chaudhary, A.; Dhiman, V.K.; Kumar, A.; Goyal, A. Impact of dry sewage sludge on characteristics of concrete. *Mater. Today Proc.* **2022**, *52*, 818–824. [CrossRef]
17. Mojapelo, K.S.; Kupolati, W.K.; Ndambuki, J.M.; Sadiku, E.R.; Ibrahim, I.D.; Maepa, C. Sustainable usage and the positive environmental impact of wastewater dry sludge-based concrete. *Results Mater.* **2022**, *16*, 100336. [CrossRef]
18. Xia, Y.; Liu, M.; Zhao, Y.; Chi, X.; Lu, Z.; Tang, K.; Guo, J. Utilization of sewage sludge ash in ultra-high performance concrete (UHPC): Microstructure and life-cycle assessment. *J. Environ. Manag.* **2023**, *326*, 116690. [CrossRef]
19. Mun, K.J. Development and tests of lightweight aggregate using sewage sludge for nonstructural concrete. *Constr. Build. Mater.* **2007**, *21*, 1583–1588. [CrossRef]
20. Lau, P.C.; Teo, D.C.L.; Mannan, M.A. Characteristics of lightweight aggregate produced from lime-treated sewage sludge and palm oil fuel ash. *Constr. Build. Mater.* **2017**, *152*, 558–567. [CrossRef]
21. Chang, Z.; Long, G.; Xie, Y.; Zhou, J.L. Pozzolanic reactivity of aluminum-rich sewage sludge ash: Influence of calcination process and effect of calcination products on cement hydration. *Constr. Build. Mater.* **2022**, *318*, 126096. [CrossRef]
22. Song, Y.; Chetty, K.; Garbe, U.; Wei, J.; Bu, H.; O'moore, L.; Jiang, G. A novel granular sludge-based and highly corrosion-resistant bio-concrete in sewers. *Sci. Total Environ.* **2021**, *791*, 148270. [CrossRef] [PubMed]
23. Li, X.; He, C.; Lv, Y.; Jian, S.; Jiang, W.; Jiang, D.; Dan, J. Effect of sintering temperature and dwelling time on the characteristics of lightweight aggregate produced from sewage sludge and waste glass powder. *Ceram. Int.* **2021**, *47*, 33435–33443. [CrossRef]
24. Zhang, Y.; Yu, L.; Wang, J.; Mao, H.; Cui, K. Microstructure and mechanical properties of high strength porous ceramics with high sewage sludge content. *J. Clean. Prod.* **2022**, *380*, 135084. [CrossRef]
25. Jiao, Z.; Wang, Y.; Zheng, W.; Huang, W. Effect of the activator on the performance of alkali-activated slag mortars with pottery sand as fine aggregate. *Constr. Build. Mater.* **2019**, *197*, 83–90. [CrossRef]
26. Xie, J.; Liu, J.; Liu, F.; Wang, J.; Huang, P. Investigation of a new lightweight green concrete containing sludge ceramsite and recycled fine aggregates. *J. Clean. Prod.* **2019**, *235*, 1240–1254. [CrossRef]
27. Tang, Z.; Li, W.; Tam, V.W.; Luo, Z. Investigation on dynamic mechanical properties of fly ash/slag-based geopolymeric recycled aggregate concrete. *Compos. Part B Eng.* **2020**, *185*, 107776. [CrossRef]
28. Luo, X.; Xu, J.Y.; Bai, E.L.; Li, W. Research on the dynamic compressive test of highly fluidized geopolymer concrete. *Constr. Build. Mater.* **2013**, *48*, 166–172. [CrossRef]
29. Kong, L.; Zhao, W.; Xuan, D.; Wang, X.; Liu, Y. Application potential of alkali-activated concrete for antimicrobial induced corrosion: A review. *Constr. Build. Mater.* **2022**, *317*, 126169. [CrossRef]
30. Yao, W.; Shi, Y.; Xia, K.; Peterson, K. Dynamic fracture behavior of alkali-activated mortars: Effects of composition, curing time and loading ratio. *Eng. Fract. Mech.* **2019**, *208*, 119–130. [CrossRef]
31. Wang, X.; Cui, J.; Shen, J.H.; Wang, X.Z.; Zhu, C.Q. Particle breakage behavior of a foundation filling material on island-reefs in the South China Sea under impact loading. *Bull. Eng. Geol. Environ.* **2022**, *81*, 345. [CrossRef]
32. Wang, X.; Wang, Y.; Liao, C.; Cui, J.; Shen, J.H.; Wang, X.Z.; Zhu, C.Q. Particle breakage mechanism and particle shape evolution of calcareous sand under impact loading. *Bull. Eng. Geol. Environ.* **2022**, *81*, 372. [CrossRef]

33. *ASTM C109/C109M-2011a*; Standard Test Method for Compressive Strength of Hydraulic Cement Mortars (using 2-in. or [50-mm] Cube Specimens). ASTM International: Philadelphia, PA, USA, 2011.
34. Xie, H.; Yang, L.; Zhang, Q.; Huang, C.; Chen, M.; Zhao, K. Research on energy dissipation and damage evolution of dynamic splitting failure of basalt fiber reinforced concrete. *Constr. Build. Mater.* **2022**, *330*, 127292. [CrossRef]